J Mater Sci (2019) 54:14845–14858

Energy materials

Three-dimensional MoS_2/rGO nanocomposites with homogeneous network structure for supercapacitor electrodes

Jun Bao[1,2], Xiao-Fei Zeng[1,2,*], Xie-Jun Huang[1,2], Ri-Kui Chen[1,2], Jie-Xin Wang[1,2,3], Liang-Liang Zhang[2,*], and Jian-Feng Chen[1,2,3]

[1] State Key Laboratory of Organic-Inorganic Composites, Beijing University of Chemical Technology, Beijing 100029, People's Republic of China

[2] Research Center of the Ministry of Education for High Gravity Engineering and Technology, Beijing University of Chemical Technology, Beijing 100029, People's Republic of China

[3] Beijing Advanced Innovation Center for Soft Matter Science and Engineering, Beijing University of Chemical Technology, Beijing 100029, People's Republic of China

Received: 25 May 2019
Accepted: 22 August 2019
Published online: 6 September 2019

ABSTRACT

Molybdenum disulfide/graphene (MoS_2/rGO) nanocomposites are a promising candidate for energy storage materials. However, it is still a challenge to uniformly disperse MoS_2 on rGO nanosheets, which the performance mainly depends on. In this work, we demonstrate a novel method to synthesize the three-dimensional (3D) MoS_2/rGO nanocomposites by the high-gravity reactive precipitation in a rotating packed bed (RPB) reactor combined with the hydrothermal method. The prepared nanocomposites have higher purity and larger specific surface area than that prepared in the traditional stirred tank reactor (STR). More importantly, MoS_2 is uniformly and densely dispersed on rGO nanosheets, resulting in the formation of an even 3D network structure and contributing to the achievement of excellent energy storage performance. The specific capacitance of the nanocomposites reaches 294 F g^{-1} at a scan rate of 20 mV s^{-1}, which is obviously higher than that of pure MoS_2 (122 F g^{-1}) and rGO (23 F g^{-1}). The calculated energy density and power density are 57 Wh kg^{-1} and 50 W kg^{-1}, respectively. Moreover, the preparation process is environmentally friendly, controllable and suitable for a large-scale production, which is significantly important for the development of the electrode materials applied in the supercapacitors.

Address correspondence to E-mail: zengxf@mail.buct.edu.cn; zhangll@mail.buct.edu.cn

https://doi.org/10.1007/s10853-019-03957-z

Abbreviations

RPB	Rotating packed bed
STR	Stirred tank reactor
MoS_3/GO	Molybdenum trisulfide/graphene oxide nanocomposites
MoS_2/rGO	Molybdenum disulfide/graphene nanocomposites
MoS_2/rGO-R	Molybdenum disulfide/graphene nanocomposites prepared by RPB
MoS_2/rGO-S	Molybdenum disulfide/graphene nanocomposites prepared by STR
C_{sp}	Gravimetric specific capacitance

Introduction

Owing to the rapid depletion of non-renewable resources and the environmental pollution caused by conventional energy sources, there is an urgent need for environmentally friendly and high-performance energy storage devices in recent years [1–3]. Supercapacitor has attracted a tremendous interest because of its advantages in high power density, long cyclic stability and ultrafast charge–discharge rate, which is considered to be one of the most promising electrochemical energy storage devices for a wide range of applications, including portable electronics, backup power supply, regenerative braking system, motor starter, etc. [4–6]. Supercapacitor is mainly composed of electrode, electrolyte, diaphragm and shell. The charge storage mechanisms and performance of supercapacitors are primarily governed by the electrode materials [7, 8]. Hence, the development of a facile approach for the large-scale and controllable synthesis of the electrode materials with excellent energy storage properties is very important for the wide application of supercapacitors.

Molybdenum disulfide (MoS_2), a typical transition-metal sulfide, has attracted widespread attention due to its unique physical and chemical properties [9–11]. The sheet-like morphology of MoS_2 provides a large surface area to facilitate the double-layer charge storage [12]. Meanwhile, MoS_2 presents pseudocapacitance by the intercalation of electrolyte ions into S–Mo–S nanosheets due to the multiple oxidation states of Mo atoms, which plays an important role in enhancing the charge storage behavior [13]. However, MoS_2 suffers from the intrinsically poor electrical conductivity, thus leading to a low specific capacitance, which restricts its application as energy storage materials alone [14–16]. Taking advantage of the extraordinary electronic behavior, graphene has been employed to hybridize with MoS_2 to enhance the electrical conductivity and increase the specific capacitance [17, 18]. The introduction of graphene as a template can facilitate electron transport through MoS_2 nanostructures and maximize the charge storage capability [19, 20]. Thus, the molybdenum disulfide/graphene (MoS_2/rGO) nanocomposites hold promise as supercapacitor electrode materials [21].

The methods of the synthesis of MoS_2/rGO nanocomposites are hydrothermal method [22–24], liquid exfoliation method [25], layer-by-layer technique [26], microwave heating [27–29] or laser writing [30, 31]. Among them, the hydrothermal method is widely accepted because of its simple operation. Thangappan et al. [23] presented an optimized process for in situ formation of MoS_2 on graphene sheets by the hydrothermal method. The nanocomposite shows a higher specific capacitance (270 F g^{-1} at 0.1 A g^{-1}) than pure MoS_2. However, in the formation process of MoS_2 nanosheets, the growth rate is very fast due to the formation of large quantity of unstable MoS_2 nuclei with high surface energy [23], which makes it difficult to control the growth process of MoS_2, resulting in the uneven distribution and agglomeration of MoS_2 nanosheets. Therefore, it remains a great challenge to controllably synthesize the MoS_2/rGO with good dispersion and appropriate coverage density of MoS_2 on rGO nanosheets during the hydrothermal process, which is very important for the large-scale production of MoS_2/rGO nanocomposites with excellent electrochemical performance.

Herein, we proposed a novel process of the high-gravity reactive precipitation coupled with hydrothermal reduction process to prepare the MoS_2/rGO nanocomposites with uniform three-dimensional (3D) network structure. Firstly, molybdenum trisulfide/graphene oxide (MoS_3/GO) nanocomposites were synthesized by the high-gravity technology using a rotating packed bed (RPB) reactor, and then, both of MoS_3 and GO were reduced to obtain the MoS_2/rGO nanocomposites in the hydrothermal process. In this way, the MoS_2 nanosheets are evenly and densely dispersed on rGO, which contributes to the formation of a homogeneous

3D conductive network for the achievement of the excellent energy storage performance. Remarkably, the specific capacitance of MoS_2/rGO nanocomposites reaches 294 F g^{-1} at a scan rate of 20 mV s^{-1}, which is greater than that prepared by the traditional stirred tank reactor (STR) (218 F g^{-1}), indicating the superiority of adopting RPB to synthesize MoS_2/rGO nanocomposites.

Experimental

Materials

Heptamolybdate ammonium tetrahydrate ($(NH_4)_6Mo_7O_{24}{\cdot}4H_2O$), L-cysteine ($C_3H_7NO_2S$), potassium permanganate ($KMnO_4$), hydrogen peroxide (H_2O_2, 35%) were purchased from Sinopharm Chemical Reagent Co., Ltd. (Shanghai, China). Sodium sulfide nonahydrate ($Na_2S{\cdot}9H_2O$), sulfuric acid (H_2SO_4), nitric acid (HNO_3), hydrochloric acid (HCl), ammonium hydroxide ($NH_3{\cdot}H_2O$) were purchased from Beihua Fine Chemicals Co., Ltd. (Beijing, China). All reactants were of analytical purity and used as received. Deionized water was used throughout the experiments.

Preparation of GO dispersion

GO was prepared from natural graphite via a modified Hummers' method [32]. After freeze-drying the GO product, 100 mg of GO was dissolved into 400 mL deionized water with the aid of ultrasound for 2 h; then, the fresh GO dispersion was formed for further use.

Preparation of MoS_3/GO nanocomposites

MoS_3/GO nanocomposites were synthesized via high-gravity technology. The experimental setup for the synthesis of MoS_3/GO nanocomposites is schematically shown in Fig. 1.

In a typical synthesis, 100 mL $(NH_4)_6Mo_7O_{24}{\cdot}4H_2O$ aqueous solution was added dropwise into 400 mL fresh GO dispersion in tank A under continuous stirring for 30 min. Then, the mixture and 100 mL $Na_2S{\cdot}9H_2O$ aqueous solution (in tank B) were introduced into RPB at the flow rate of 100 mL min^{-1} and 20 mL min^{-1}, respectively. The mass ratio of raw materials $(NH_4)_6Mo_7O_{24}{\cdot}4H_2O$ to GO was 10 or 15. After a period of reaction, 40 mL HCl solution (9.0 mol L^{-1}, tank C) and the resulted mixture (collection chamber in tank D) were pumped into RPB with the flow rate of 150 mL min^{-1} and 10 mL min^{-1}, respectively. After the HCl solution was exhausted, the products were pumped into RPB in a recycling mode, which was processed for 30 min. In this process, the rotating speed of RPB was set to 1500 rpm and the jacket temperature of RPB was maintained at 40 °C. Finally, 70 mL brownish-red MoS_3/GO suspension was collected for the further reaction.

For comparison, a similar process was performed in STR. The solution from tank A, tank B and tank C was pumped successively into tank D at 40 °C under continuous stirring. After that, the resultant mixture was stirred for another 30 min to obtain the brownish-red MoS_3/GO dispersion.

Preparation of MoS_2/rGO nanocomposites

To convert the MoS_3/GO nanocomposites into the MoS_2/rGO nanocomposites, the synthesized 70 mL MoS_3/GO suspension was first mixed with 1.0 g L-cysteine. Then, the pH of the solution was adjusted to 4.50. Finally, the mixture was transferred into a 150-mL Teflon-lined stainless-steel autoclave and heated at 200 °C for 24 h. After cooling to room temperature, the obtained black precipitate was washed with ethanol and water and freeze-dried for further characterizations. For comparison, bare MoS_2 and rGO samples were also prepared under the same conditions.

For the convenience of expression, we will simply refer to the synthesized MoS_3/GO nanocomposites by STR or RPB as MoS_3/GO-S and MoS_3/GO-R, and the synthesized MoS_2/rGO nanocomposites by STR or RPB at the mass ratio of raw materials $(NH_4)_6Mo_7O_{24}{\cdot}4H_2O$ to GO of 10 and 15 as MoS_2/rGO-S10, MoS_2/rGO-S15, MoS_2/rGO-R10 and MoS_2/rGO-R15, respectively.

Characterization

The crystal structure of the materials was determined using Bruker D8 Advance X-ray diffractometer (XRD) equipped with a CuKα tube. Transmission electron microscopy (TEM) images were obtained with Hitachi HT7700 EXALENS. High-resolution transmission electron microscopy (HRTEM) images and selected

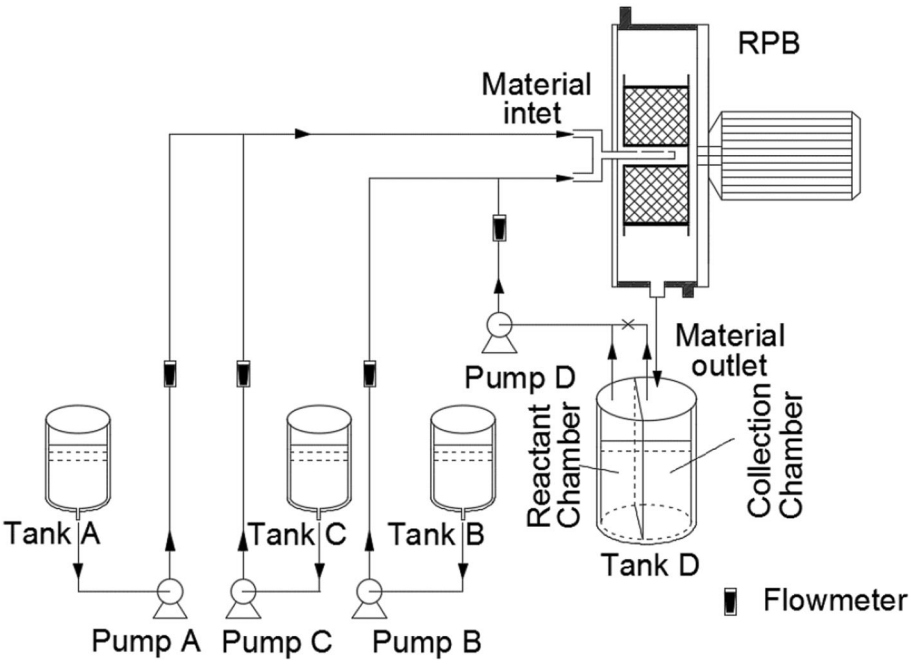

Figure 1 Schematic diagram of experimental setup for the synthesis of MoS_3/GO nanocomposites.

area electron diffraction (SAED) patterns were studied using Hitachi HR9500. X-ray photoelectron spectroscopy (XPS) analysis was performed using a Thermo ESCALAB 250 X-ray photoelectron spectrophotometer with an Al Kα anode (300 W). The surface morphology of MoS_2/rGO nanocomposites was characterized by scanning electron microscopy (SEM) (Hitachi S-4700, Japan). The specific surface area was determined by Brunauer–Emmett–Teller (BET) measurements using an ASAP2020 surface area analyzer.

Electrochemical measurements were taken on a CHI 760E electrochemical workstation with a standard three-electrode system at room temperature. A platinum foil electrode and an Ag/AgCl electrode were used as the counter and reference electrodes, respectively. The electrolyte was 1 M Na_2SO_4 aqueous solution. The working electrode was prepared by mixing the MoS_2/rGO nanocomposites, ethanol and Nafion solution in appropriate proportion to obtain an optimum viscous suspension. The resulted slurry was casted on a glassy carbon electrode and dried for 30 min under ambient condition. The electrochemical measurements were characterized with a potential range of − 0.8 to 0.2 V. Cyclic voltammetry (CV), galvanostatic charge–discharge (GCD), cyclic stability and electrochemical impedance spectroscopy (EIS) measurements were taken to evaluate the electrochemical performance. Before all electrochemical experiments, the working electrodes were activated by the cyclic voltammetry method with a scanning rate of 100 mV s^{-1} for 500 circles. The gravimetric specific capacitance (C_{sp}, F g^{-1}) of the samples was calculated from the CV curves using Eq. (1) [33, 34].

$$C_{sp} = \frac{\int I dV}{m \cdot \Delta V \cdot v} \quad (1)$$

where I is the response current (A), m is the active mass of the electrode material (g), v is the potential scan rate (V s^{-1}) and ΔV is the potential window (V).

Results and discussion

Formation process and principle of MoS_2/rGO nanocomposites

The schematic illustration of the preparation process for MoS_2/rGO-R nanocomposites is given in Fig. 2. In brief, the entire process is divided into two steps: preparation of MoS_3/GO nanocomposites by high-gravity reactive precipitation method and preparation of MoS_2/rGO nanocomposites by hydrothermal reduction of MoS_3/GO.

In the first step, MoS_3 nanoparticles were synthesized via an in situ reaction and deposited on GO due to the interactions between functional groups on GO sheets and Mo precursors [35]. The reactions were taken place in RPB, and the equations are shown in

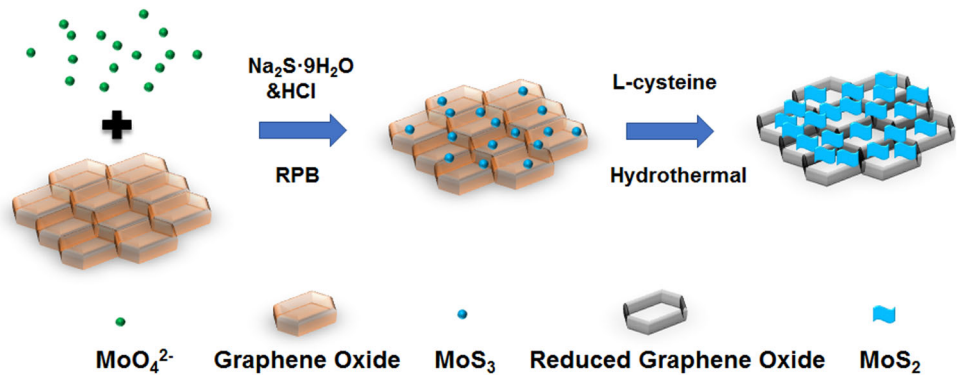

Figure 2 Schematic illustration of the preparation process for MoS_2/rGO nanocomposites.

Formula (2) [36]. In the raw materials solution, the pH value of the resultant mixture was about 12, and Mo(VI) ions were existed in the form of MoO_4^{2-} [37]. When $Na_2S{\cdot}9H_2O$ was added, the released S^{2-} would combine with MoO_4^{2-} to form MoS_4^{2-}. Then, MoS_3 nuclei attached on the surface of GO were formed after the addition of HCl.

$$\begin{aligned} MoO_4^{2-} + 4S^{2-} + 4H_2O &\rightleftharpoons MoS_4^{2-} + 8OH^- \\ MoS_4^{2-} + 2H^+ &\rightarrow MoS_3 \downarrow + H_2S \uparrow \end{aligned} \quad (2)$$

In the second step, MoS_3 nanoparticles continued to grow and were simultaneously reduced to MoS_2 nanosheets during the hydrothermal process. GO was also reduced to rGO by L-cysteine at the same time. Eventually, the MoS_2/rGO nanocomposites with the morphology of MoS_2 nanosheets uniformly standing on rGO were synthesized.

According to the studies [38, 39], in the first step, the induction time of MoS_3 nucleation (τ) is usually within 1 ms. In order to obtain MoS_3 distributed on rGO uniformly, it is necessary to ensure that the reaction environments of the system, such as the concentration, temperature and supersaturation, are homogeneous before nucleation. However, in the traditional STR, the characteristic time of micro-mixing (t_m) is estimated to be on the order of 5–50 ms, which is obviously greater than τ. So the reaction environments cannot be completely uniform before the nucleation of MoS_3, indicating that it is difficult to achieve the uniform distribution of MoS_3 nuclei on GO. According to our previous research [40, 41], RPB can intensify micro-mixing and mass transfer effectively in the reaction system. The t_m of RPB is estimated to be 0.01–0.1 ms, which is smaller than τ. Therefore, the MoS_3/GO nanocomposites are suitable for synthesis in RPB to finely control the size, dispersity and coverage density of MoS_3 on GO sheets, especially for the large-scale production. In this way, the distribution of MoS_2 nanosheets on rGO during hydrothermal process can be precisely controlled.

Structure and composition of samples

Figure 3a, b is the TEM image of the prepared MoS_3/GO-R and MoS_2/rGO-R nanocomposites, respectively. As can be seen from Fig. 3a, the MoS_3 nanoparticles with irregular shapes are densely and uniformly distributed on the surface of GO sheets. Figure 3b exhibits the sheet-like MoS_2 homogeneously anchored on rGO substrates. The average longitudinal length of the MoS_2 nanosheets is about 85 nm, and no MoS_2 agglomeration can be observed in the nanocomposites. From the SEM image of the MoS_2/rGO-R in Fig. 3c, it can also be seen that MoS_2 is uniformly distributed, densely arranged and interlaced on the surface of rGO to form an obvious 3D mesh structure [42]. The HRTEM image of MoS_2/rGO-R (Fig. 3d) shows that MoS_2 nanosheets have a hierarchical crystal lattice structure with an interlayer distance of 0.93 nm. Each MoS_2 nanosheet is composed of 4–6 layers, which is lower than pure MoS_2 (tens of layers) [43, 44], indicating that rGO inhibits the restacking of MoS_2 layers [42]. The d-spacing value of MoS_2 nanosheets is 0.26 nm, which can be ascribed to the (100) plane of MoS_2 [45]. In addition, the clearly visible and non-overlapping lattice of MoS_2 indicates that MoS_2 nanosheets are perpendicular to rGO. The crystalline structure of MoS_2/rGO-R was also investigated by the SAED pattern, as shown in Fig. 3e. Four diffraction rings attributed to the (002), (100), (103) and (110) planes of MoS_2 can be obviously observed, indicating the formation of pure hexagonal phase of MoS_2 [46].

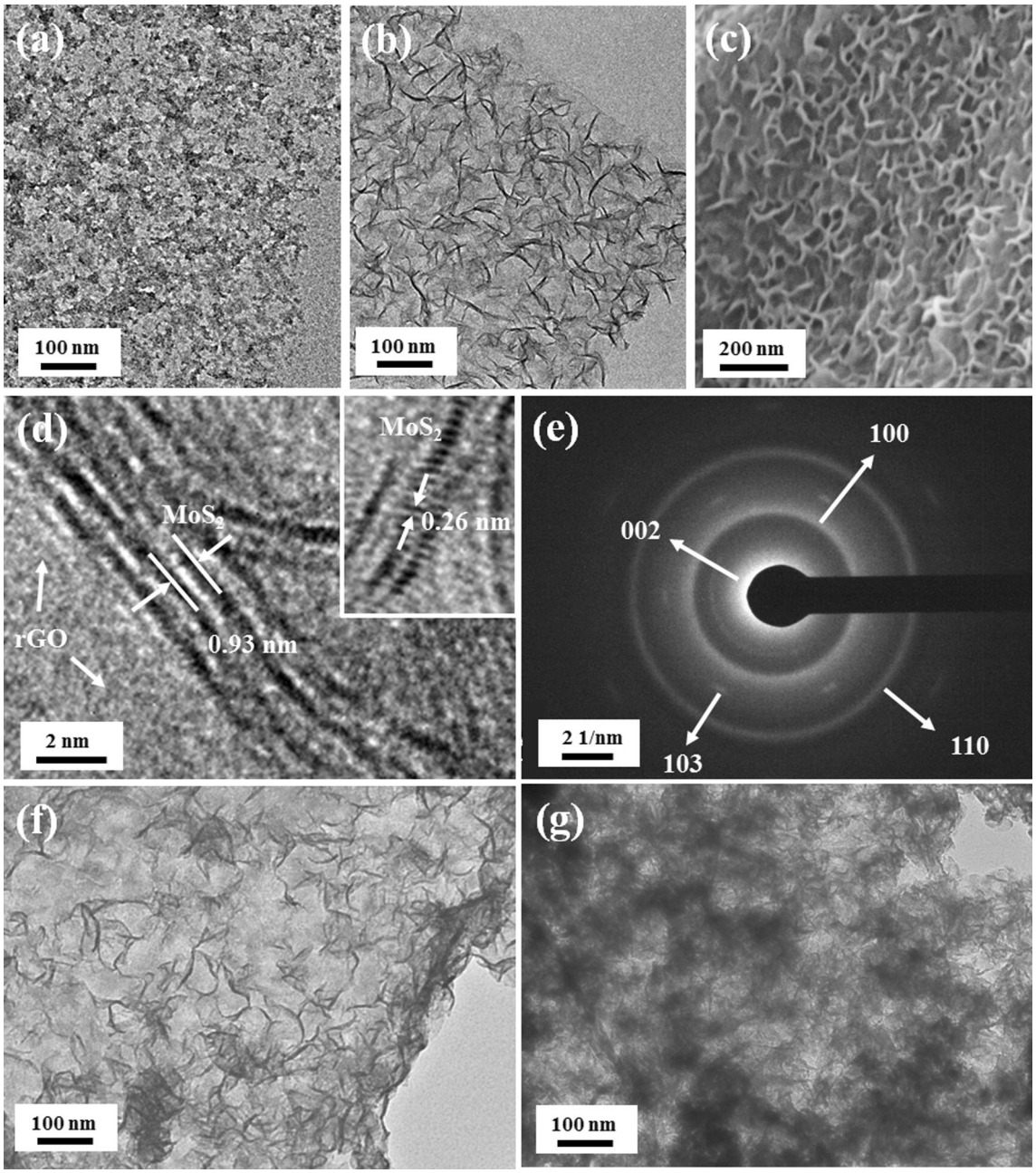

Figure 3 **a** TEM image of MoS_3/GO-R. **b** TEM image of MoS_2/rGO-R. **c** SEM image of MoS_2/rGO-R. **d** HRTEM image of MoS_2/rGO-R and the details of the MoS_2 in the inset. **e** Typical SAED pattern of MoS_2/rGO-R. **f** TEM image of MoS_2/rGO-S10. **g** TEM image of MoS_2/rGO-R15.

Figure 3f is the TEM image of the MoS_2/rGO-S nanocomposites synthesized by the traditional stirring method. The MoS_2 nanosheets are unevenly distributed on the surface of rGO. Some MoS_2 nanosheets are sparsely distributed, and some are densely distributed and even agglomerated. Figure 3g shows the TEM image of MoS_2/rGO-R15. Comparing the morphology between MoS_2/rGO-R10 (Fig. 3b) and MoS_2/rGO-R15 (Fig. 3g), it can be obviously seen that when the mass ratio of $(NH_4)_6Mo_7O_{24}{\cdot}4H_2O$ to GO is increased from 10 to 15, the loading of MoS_2 on rGO increases remarkably, resulting in excessive stacking and partially agglomeration of MoS_2 on rGO.

The nitrogen adsorption/desorption isotherms of MoS_2/rGO-R10 and MoS_2/rGO-S10 nanocomposites

are shown in Fig. 4. Both samples show the type-II isotherms with hysteresis loop. The desorption hysteresis at the relative pressure between 0.2 and 0.9 reveals that the porosities of the nanocomposites are mainly composed of mesoporous [42]. The BET specific surface area of MoS_2/rGO-S10 is calculated to be 75 $m^2 g^{-1}$, which is only 62% of MoS_2/rGO-R10 (121 $m^2 g^{-1}$). In addition, the MoS_2/rGO-R10 has an average pore size of 3.8 nm, which is larger than MoS_2/rGO-S10 (2.4 nm). Therefore, the uneven distribution of MoS_2 nanosheets on the surface of rGO synthesized in STR might lead to the decrease in the specific surface area of MoS_2/rGO-S10. The specific surface area of MoS_2/rGO-R15 reaches 133 $m^2 g^{-1}$. However, the larger specific surface area of MoS_2/rGO-R15 than MoS_2/rGO-R10 does not seem to increase the specific capacitance, as discussed in Electrochemical Characterization section.

Figure 5 shows XRD patterns of GO, MoS_2 and MoS_2/rGO-R nanocomposites. The strong and sharp diffraction peak of GO at 11.0° is corresponded to the (001) crystallographic plane, and this plane is disappeared in the pattern of MoS_2/rGO-R nanocomposites, revealing the reduction of GO during the hydrothermal process [23]. The diffraction peaks at 13.3°, 33.0°, 40.1° and 58.3° of MoS_2 are assigned to the (002), (100), (103), (110) crystallographic planes of the hexagonal phase MoS_2 (JCPDS No. 37-1492) [47]. From the XRD pattern of MoS_2/rGO-R, the peak attributed to (002) plane of MoS_2 cannot be seen and only two peaks attributed to (100) and (110) planes can be found. This fact indicates that rGO inhibits the growth of the (002) plane MoS_2 crystal, resulting in the reduction in the number of layers of MoS_2 nanosheets [48], as can be seen from the HRTEM image. The two new diffraction peaks of MoS_2/rGO-R located at 9.0° and 17.5° are named as α and β, which are indexed to neither MoS_2 nor rGO. The d-spacing corresponding to α and β peaks should be attributed to the interlayer distance of adjacent MoS_2 nanosheets on rGO and the spacing between the MoS_2 layer and the rGO layer, respectively [17, 33].

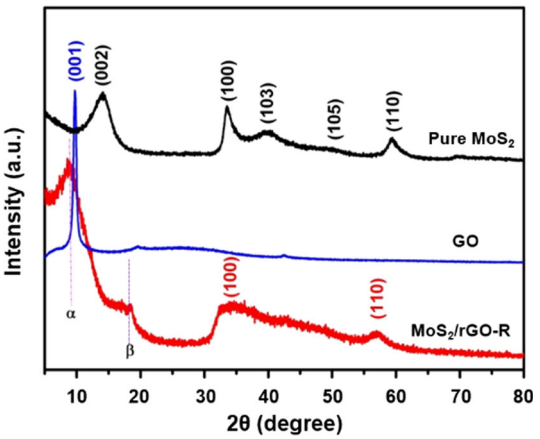

Figure 5 XRD patterns of pure MoS_2, GO and MoS_2/rGO-R nanocomposites.

Figure 6 shows the Raman spectra related to GO, MoS_2 and MoS_2/rGO-R nanocomposites. Two peaks at 1356 cm^{-1} and 1588 cm^{-1} are corresponded to D and G bands of graphene [49]. D band represents the defects nature of graphene, and the G band represents the structure ordering of graphene associating with the sp^2 carbon atom E_{2g} vibration mode [50, 51]. From Fig. 6, it can be seen that the intensity ratio of D and G bands (I_D/I_G) is less than 1 for GO and above 1 for MoS_2/rGO-R, which demonstrates that a mass

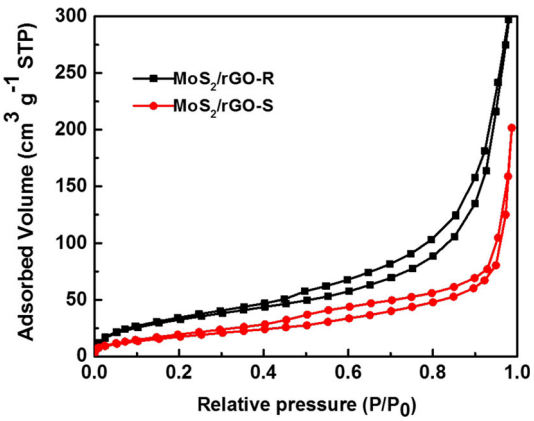

Figure 4 Nitrogen adsorption isotherms of MoS_2/rGO-R10 and MoS_2/rGO-S10 nanocomposites.

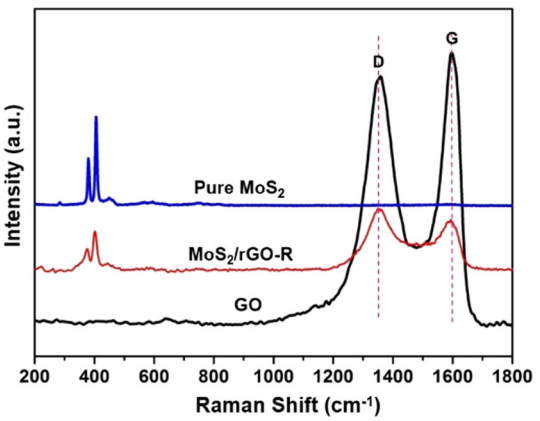

Figure 6 Raman spectroscopy of pure GO, pure MoS_2 and MoS_2/rGO-R.

defects are introduced into the structure during the reduction process of GO to rGO [52]. In the MoS_2 spectrum, only the peaks at 376 and 402 cm^{-1} are observed, indicating that the typical 2H phase of MoS_2 is synthesized [9]. The corresponding two peaks of MoS_2/rGO-R nanocomposites are slightly shifted to low frequencies (373 cm^{-1} and 400 cm^{-1}), resulting from the decreased number of layers of MoS_2 nanosheets [23], as confirmed by HRTEM and XRD characterization.

In order to further understand the chemical composition and atom valence states of the MoS_2/rGO nanocomposites, XPS analysis was performed. The XPS spectrum of MoS_2/rGO-R is shown in Fig. 7a. The characteristic peaks at 161 eV, 230 eV, 285 eV and 532 eV are corresponded to the binding energy of S 2*p*, Mo 3*d*, C 1*s* and O 1*s* [44]. Figure 7b is the high-resolution XPS spectrum of C 1*s* of MoS_2/rGO-R. The C 1*s* peak is composed of C–C/C=C, C–O and OH–C=O species at 284.6, 285.7 and 289.0 eV, respectively. Figure 7c, d shows Mo 3*d* XPS survey of MoS_2/rGO-R and MoS_2/rGO-S, respectively. Two dominant peaks at 231.6 and 228.4 eV in both figures are assigned to Mo $3d_{3/2}$ and Mo $3d_{5/2}$ binding energies. The valence of Mo in MoS_2/rGO-R nanocomposites is all Mo(IV) without other valences. However, the peaks of Mo 3*d* XPS spectrum of MoS_2/rGO-S at 235.9 eV and 229.5 eV are the characteristic peaks of Mo(VI) and Mo(V), respectively, which indicates that MoS_3 prepared by the traditional stirring method is not completely reduced. The distribution of MoS_3 nanoparticles on GO prepared by RPB is more homogeneous than that prepared by STR, so the MoS_3 nanoparticles are more uniformly and sufficiently contacted with the reducing agent, and finally Mo(VI) is more completely reduced during the hydrothermal process. Obviously, the purity of MoS_2/rGO-R is higher than that of MoS_2/rGO-S, resulting in that the electrochemical performance of MoS_2/rGO-S is inferior to that of MoS_2/rGO-R due to the presence of Mo(VI) and Mo(V) impurities.

Electrochemical characterization

The electrochemical performance of rGO, MoS_2 and MoS_2/rGO was evaluated by CV and GCD measurements. Figure 8a–c shows the CV curves of the electrodes made from rGO, MoS_2 and MoS_2/rGO-R with the scanning rate from 20 to 100 mV s^{-1}, respectively. Generally, the current density increases as the scanning rate increases. The curves of pure rGO electrode achieve rectangular shapes, which is a

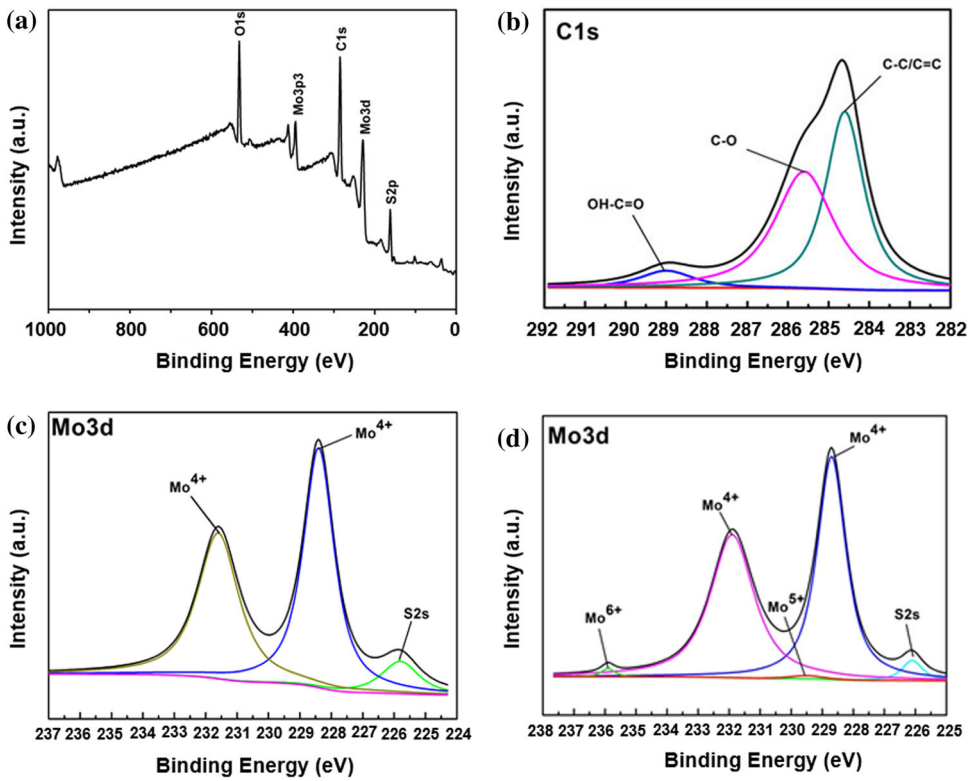

Figure 7 **a** Wide XPS spectrum of MoS_2/rGO-R. **b** C 1*s* deconvolution spectra and **c** Mo 3*d* deconvolution spectra of MoS_2/rGO-R. **d** Mo 3*d* deconvolution spectra of MoS_2/rGO-S.

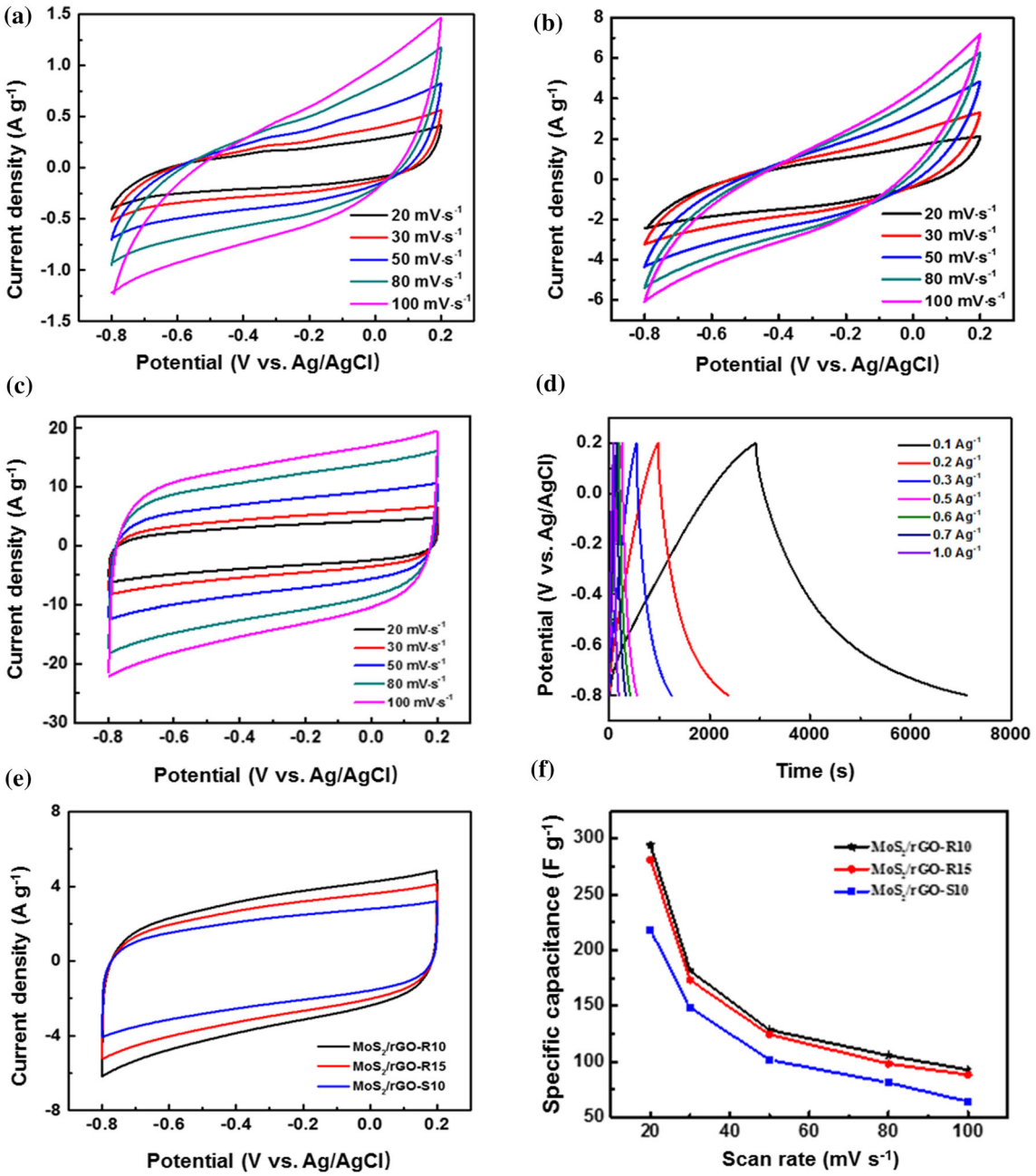

Figure 8 CV curves of **a** pure rGO, **b** pure MoS_2, **c** MoS_2/rGO-R modified electrode at different scan rates (20, 30, 50, 80, 100 mV s^{-1}) in 1 M Na_2SO_4 aqueous solution. **d** Galvanostatic charge–discharge curves of MoS_2/rGO-R at different current densities (0.1, 0.2, 0.3, 0.5, 0.6, 0.7 and 1 A g^{-1}). **e** CV curves comparison of MoS_2/rGO-S10, MoS_2/rGO-R10 and MoS_2/rGO-R15 at a scan rate of 20 mV s^{-1}. **f** Specific capacitance of MoS_2/rGO-R10, MoS_2/rGO-R15 and MoS_2/rGO-S10 nanocomposites at different scan rates.

characteristic of an ideal double-layer capacitor [53, 54]. The MoS_2 electrode also shows near-rectangular curved shapes without obvious redox peaks, resulting from that the double-layer capacitive behavior of MoS_2 is exhibited at high scan rates of more than 20 mV s^{-1} [13]. The CV curves of MoS_2/rGO-R electrode show quasi-rectangular and symmetrical shapes, indicating that MoS_2/rGO mainly follows the double-layer capacitance mechanism. The integral area of the CV curves of MoS_2/rGO-R nanocomposites electrode is higher than that of bare MoS_2 and rGO, indicating a higher specific

capacitance. The improvement in electrochemical performance is mainly attributed to the synergistic effects of MoS_2 and rGO sheets [23]. The rGO matrix facilitates the dispersion of MoS_2 nanosheets and acts as a highly conductive current collector and an active interface center for enhancing the electrical conductivity, and the large specific surface area of MoS_2 nanosheets with nanoscale size can reduce the diffusion length of ions and increase the diffusion rate of ions [55].

Figure 8d is the GCD curve of the MoS_2/rGO-R electrode within the voltage window of − 0.8 to 0.2 V. All the curves are approximately linear and symmetrical at different current densities, which validated the good reversibility of MoS_2/rGO-R electrode [44]. Figure 8e shows the comparison of the typical CV curves of MoS_2/rGO-S10, MoS_2/rGO-R10 and MoS_2/rGO-R15 at the same scan rate. From these CV curves, the specific capacitances of them are calculated according to Eq. (1), as shown in Fig. 8f. It is proved that the capacitance properties of MoS_2/rGO prepared by RPB are obviously superior to that of MoS_2/rGO prepared by STR, mainly resulting from the higher purity and the formation of uniform 3D network structure as mentioned above. When the scan rate is 20 mV s^{-1}, the specific capacitance of MoS_2/rGO-R10 (294 F g^{-1}) is 1.35 times of MoS_2/rGO-S10. Moreover, the capacitance performance of MoS_2/rGO-R10 is better than MoS_2/rGO-R15 possessed a larger specific surface area. The main reason is that the agglomerated MoS_2 nanosheets of MoS_2/rGO-R15 nanocomposites reduce the electrochemical utilization efficiency of MoS_2, thereby reducing the synergy between MoS_2 and rGO [44, 56]. Therefore, the dispersion state of MoS_2 nanosheets has a great influence on the electrochemical performance of the nanocomposites.

Table 1 shows the comparison of the electrochemical performance of MoS_2/rGO nanocomposite electrodes prepared in our work and reported in the studies [20, 22, 23, 26]. The specific capacitance of MoS_2/rGO-R nanocomposites is superior to that of the previously reported materials. More importantly, the ratios of the specific capacitances of the nanocomposites to the pure rGO and MoS_2 in this work are 12.8 and 2.4 times, respectively, obviously higher than that reported in the studies. This indicates that the MoS_2/rGO nanocomposites synthesized by the high-gravity technology have a better synergistic effect between rGO and MoS_2.

The cycling stability of the prepared MoS_2/rGO-S and MoS_2/rGO-R nanocomposites was carried out at a scan rate of 20 mV s^{-1}. The specific capacitances at different cycling stages are shown in Fig. 9. It can be seen that the specific capacitance of MoS_2/rGO-S nanocomposites is 166 F g^{-1} after 2000 cycles, which is only 76% of the initial value. However, about 85% of the initial capacitance of MoS_2/rGO-R can still be retained, indicating a superior cycling performance.

EIS measurement was also taken to clarify the internal resistance of the electrode as well as the resistance between the electrode and the electrolyte. The Nyquist plots of the fabricated MoS_2/rGO-R and MoS_2/rGO-S electrodes are demonstrated in Fig. 10. MoS_2/rGO-S electrode shows an incomplete semicircle in the high-frequency region and a straight line in the low-frequency region. The incomplete semicircle is attributed to the charge transfer impedance at the electrode–electrolyte interface, and the straight line reveals the ideal capacitive behavior [57]. However, MoS_2/rGO-R does not show the semicircle region at high frequency, which is probably due to the low faradic resistance [56]. MoS_2/rGO-R exhibits a larger slope in the low-frequency region than MoS_2/rGO-S, demonstrating a faster internal ion diffusion rate. Moreover, the electron transfer resistance (R_{ct}) of MoS_2/rGO-R (4.4 Ω) is less than that of MoS_2/rGO-S (25.7 Ω), resulting from that the interconnected 3D conductive network is beneficial to improve the conductivity of MoS_2/rGO-R. All these results show that the MoS_2/rGO-R electrode with 3D structure has a lower charge transfer impedance at the electrode–electrolyte interface and a faster internal electron transport velocity than the MoS_2/rGO-S electrode. Therefore, MoS_2/rGO-R composite shows higher C_{sp} than MoS_2/rGO-S [20, 42].

Figure 11 shows the Ragone plots of MoS_2/rGO nanocomposites. The specific energy density (E) and specific power density (P) of the MoS_2/rGO electrodes are calculated according to Eqs. (3) and (4) [58, 59].

$$E = \frac{0.5 C_{sp} V^2}{3.6} \tag{3}$$

$$P = \frac{3600E}{t} \tag{4}$$

where C_{sp} (F g^{-1}) is the specific capacitance of the electrode. The values of V (V) and t (s) are taken from Fig. 8d, which represent the voltage change during the discharge process after internal resistance drop

Table 1 Comparison of electrochemical properties of different MoS_2/rGO materials for supercapacitor electrodes

Electrode materials	C_{sp} of nanocomposites (F g^{-1})	C_{sp} of rGO (F g^{-1})	C_{sp} of MoS_2 (F g^{-1})	Ratio	References
MoS_2 layers deposited on graphene	265	40	–	6.6/–	[20]
Layered MoS_2–graphene nanocomposites	243	35	120	6.9/2.0	[22]
Graphene decorated with MoS_2 nanosheets	270	–	162	–/2.2	[23]
MoS_2 nanosheet–graphene nanosheet	282	–	156	–/1.8	[26]
3D MoS_2 nanosheets coupled on graphene	294	23	122	12.8/2.4	Present work

The ratio is equal to the C_{sp} of MoS_2/rGO divided by the C_{sp} of rGO or MoS_2 electrodes

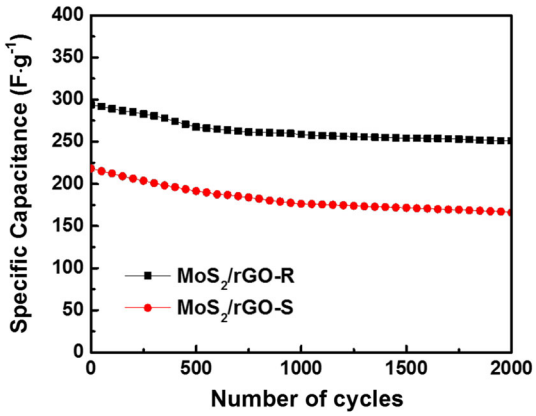

Figure 9 Cycle stability analysis of MoS_2/rGO-R and MoS_2/rGO-S at a scan rate of 20 mV s^{-1}.

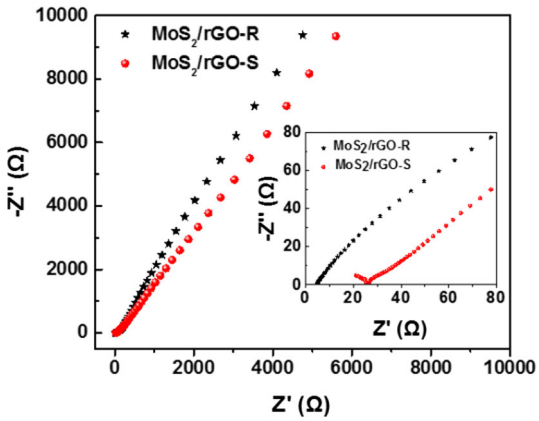

Figure 10 Impedance spectra of the as-fabricated MoS_2/rGO nanocomposites electrodes. Inset shows the high-frequency region of the impedance spectra.

and the discharge time, respectively. It can be seen from Ragone plots, the energy density gradually decreases as the power density increases and the energy density of MoS_2/rGO-R is always greater than

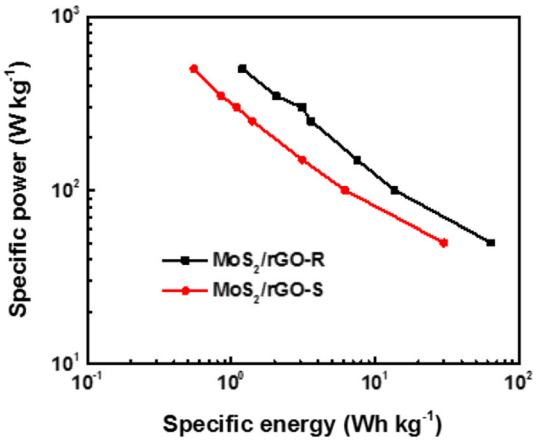

Figure 11 Ragone plots for MoS_2/rGO-R and MoS_2/rGO-S nanocomposites.

that of MoS_2/rGO-S at the same power density. When the power density is 50 W kg^{-1}, the energy density of MoS_2/rGO-R reaches 57 Wh kg^{-1}, while the energy density of MoS_2/rGO-S is only 30 Wh kg^{-1}. These results illustrate that the MoS_2/rGO-R nanocomposites have excellent electrochemical properties of high energy density and power output.

According to the results of electrochemical characterization, the superior electrochemical performance of MoS_2/rGO-R is mainly due to the synergistic effects of MoS_2 and rGO sheets, as well as the uniform 3D mesh network structure. The uniform 3D network structure helps to reduce the electron transport resistance and facilitate fast transportation of electrons through the whole electrode matrix. The formation of this unique 3D structure is attributed to the homogeneous reaction environment created by the RPB. In addition, the yield of MoS_2/rGO-R is as high as 94.3%. Therefore, the MoS_2/rGO electrode

material with excellent energy storage performance can be synthesized by RPB reactor on a large scale to meet the requirements of supercapacitor.

Conclusion

Three-dimensional MoS_2/rGO nanocomposites with homogeneous network structure are successfully synthesized by high-gravity technology and hydrothermal reduction method. When tested as an electrode, the as-obtained MoS_2/rGO-R nanocomposites exhibit high capacity and excellent rate capability. Electrochemical measurements indicate that the electrode exhibits a specific capacitance as high as 294 F g^{-1} at a scan rate of 20 mV s^{-1}. The calculated energy density and power density are 57 Wh kg^{-1} and 50 W kg^{-1}, respectively. This superior electrochemical performance is attributed to the synergistic effects between MoS_2 and rGO sheets, as well as the unique 3D mesh network architecture that reduces the electron transfer resistance and Faradic resistance. This research provides an effective procedure for the large-scale manufacturing of MoS_2/rGO by the high-gravity technology. Moreover, MoS_2/rGO nanocomposites with excellent performance are a promising candidate for electrode materials in supercapacitor electrodes and other energy storage devices.

Acknowledgements

This work was financially supported by the National Key Research and Development Program of China (2016YFA0201701/2016YFA0201700) and the National Natural Science Foundation of China (21776016).

Compliance with ethical standards

Conflict of interest The authors declare that they have no conflict of interest.

References

[1] Zhao JW, Chen J, Xu SM, Shao MF, Zhang Q, Wei F, Ma J, Wei M, Evans DG, Duan X (2014) Hierarchical NiMn layered double hydroxide/carbon nanotubes architecture with superb energy density for flexible supercapacitors. Adv Funct Mater 24:2938–2946

[2] Simon P, Gogotsi Y (2008) Materials for electrochemical capacitors. Nat Mater 7:845–854

[3] Dhibar S, Das CK (2014) Silver nanoparticles decorated polyaniline/multiwalled carbon nanotubes nanocomposite for high-performance supercapacitor electrode. Ind Eng Chem Res 53:3495–3508

[4] Simon P, Gogotsi Y, Dunn B (2014) Where do batteries end and supercapacitors begin? Science 343:1210–1211

[5] Zhu L, Zhang S, Cui Y, Song H, Chen X (2013) One step synthesis and capacitive performance of graphene nanosheets/Mn_3O_4 composite. Electrochim Acta 89:18–23

[6] Liu S, San Hui K, Hui KN, Yun JM, Kim KH (2016) Vertically stacked bilayer $CuCo_2O_4$/$MnCo_2O_4$ heterostructures on functionalized graphite paper for high-performance electrochemical capacitors. J Mater Chem A 4:8061–8071

[7] Cao X, Shi Y, Shi W, Rui X, Yan Q, Kong J, Zhang H (2013) Preparation of MoS_2-coated three-dimensional graphene networks for high-performance anode material in lithium-ion batteries. Small 9:3433–3438

[8] Wang GP, Zhang L, Zhang JJ (2012) A review of electrode materials for electrochemical supercapacitors. Chem Soc Rev 41:797–828

[9] Acerce M, Voiry D, Chhowalla M (2015) Metallic 1T phase MoS_2 nanosheets as supercapacitor electrode materials. Nat Nanotechnol 10:313–318

[10] Yang Y, Fei HL, Ruan GD, Xiang CS, Tour JM (2014) Edge-oriented MoS_2 nanoporous films as flexible electrodes for hydrogen evolution reactions and supercapacitor devices. Adv Mater 26:8163–8168

[11] Chang C, Yang X, Xiang S, Que H, Li M (2017) Layered MoS_2/PPy nanotube composites with enhanced performance for supercapacitors. J Mater Sci Mater Electron 28:1777–1784

[12] Huang KJ, Zhang JZ, Shi GW, Liu YM (2014) Hydrothermal synthesis of molybdenum disulfide nanosheets as supercapacitors electrode material. Electrochim Acta 132:397–403

[13] Soon JM, Loh KP (2007) Electrochemical double-layer capacitance of MoS_2 nanowall films. Electrochem Solid State Lett 10:A250–A254

[14] Saraf M, Natarajan K, Saini AK, Mobin SM (2017) Small biomolecule sensors based on an innovative MoS_2–rGO heterostructure modified electrode platform: a binder-free approach. Dalton Trans 46:15848–15858

[15] Yang MH, Ko S, Im JS, Choi BG (2015) Free-standing molybdenum disulfide/graphene composite paper as a binder-and carbon-free anode for lithium-ion batteries. J Power Sources 288:76–81

[16] Guo Y, Qi X, Fu X, Hu Y, Peng Z (2019) Vertically standing ultrathin MoS_2 nanosheet arrays on molybdenum foil as binder-free anode for lithium-ion batteries. J Mater Sci 54:4105–4114. https://doi.org/10.1007/s10853-018-3091-9

[17] Yang M, Jeong JM, Huh YS, Choi BG (2015) High-performance supercapacitor based on three-dimensional MoS_2/graphene aerogel composites. Compos Sci Technol 121:123–128

[18] Behranginia A, Asadi M, Liu C, Yasaei P, Kumar B, Phillips P, Foroozan T, Waranius JC et al (2016) Highly efficient hydrogen evolution reaction using crystalline layered three-dimensional molybdenum disulfides grown on graphene film. Chem Mater 28(2):549–555

[19] He P, Zhao K, Huang B, Zhang B, Huang Q, Chen T, Zhang Q (2018) Mechanically robust and size-controlled MoS_2/-graphene hybrid aerogels as high-performance anodes for lithium-ion batteries. J Mater Sci 53:4482–4493. https://doi.org/10.1007/s10853-017-1853-4

[20] Da Silveira Firmiano EG, Rabelo AC, Dalmaschio CJ, Pinheiro AN, Pereira EC, Schreiner WH, Leite ER (2014) Supercapacitor electrodes obtained by directly bonding 2D MoS_2 on reduced graphene oxide. Adv Energy Mater 4:1301380. https://doi.org/10.1002/aenm.201301380

[21] Dutta S, De S (2018) MoS_2 nanosheet/rGO hybrid: an electrode material for high performance thin film supercapacitor. Mater Today Proc 5:9771–9775

[22] Huang KJ, Wang L, Liu YJ, Liu YM, Wang HB, Gan T, Wang LL (2013) Layered MoS_2–graphene composites for supercapacitor applications with enhanced capacitive performance. Int J Hydrog Energy 38:14027–14034

[23] Thangappan R, Kalaiselvam S, Elayaperumal A, Jayavel R, Arivanandhan M, Karthikeyan R, Hayakawa Y (2016) Graphene decorated with MoS_2 nanosheets: a synergetic energy storage composite electrode for supercapacitor applications. Dalton Trans 45:2637–2646

[24] Wang M, Han X, Zhao Y, Li J, Ju P, Hao Z (2018) Tuning size of MoS_2 in MoS_2/graphene oxide heterostructures for enhanced photocatalytic hydrogen evolution. J Mater Sci 53:3603–3612. https://doi.org/10.1007/s10853-017-1745-7

[25] Huang M, Zhou Y, Guo Y, Wang H, Hu X, Xu X, Ren Z (2018) Facile one-pot liquid exfoliation preparation of molybdenum sulfide and graphene heterojunction for photoelectrochemical performance. J Mater Sci 53:7744–7754. https://doi.org/10.1007/s10853-018-2108-8

[26] Patil S, Harle A, Sathaye S, Patil K (2014) Development of a novel method to grow mono-/few-layered MoS_2 films and MoS_2–graphene hybrid films for supercapacitor applications. CrystEngComm 16:10845–10855

[27] Li J, Liu X, Pan L, Qin W, Chen T, Sun Z (2014) MoS_2–reduced graphene oxide composites synthesized via a microwave-assisted method for visible-light photocatalytic degradation of methylene blue. RSC Adv 4:9647–9651

[28] Liu N, Wang X, Xu W, Hu H, Liang J, Qiu J (2014) Microwave-assisted synthesis of MoS_2/graphene nanocomposites for efficient hydrodesulfurization. Fuel 119:163–169

[29] Ji H, Hu S, Shi S, Guo B, Hou W, Yang G (2018) Rapid microwave-hydrothermal preparation of few-layer MoS_2/C nanocomposite as anode for highly reversible lithium storage properties. J Mater Sci 53:14548–14558. https://doi.org/10.1007/s10853-018-2631-7

[30] Clerici F, Fontana M, Bianco S, Serrapede M, Perrucci F, Ferrero S, Tresso E, Lamberti A (2016) In situ MoS_2 decoration of laser-induced graphene as flexible supercapacitor electrodes. ACS Appl Mater Interfaces 8:10459–10465

[31] Castellanos-Gomez A, Barkelid M, Goossens AM, CaladoH VE, van der Zant HSJ, Steele GA (2012) Laser-thinning of MoS_2: on demand generation of a single-layer semiconductor. Nano Lett 12:3187–3192

[32] Hummers WS Jr, Offeman RE (1958) Preparation of graphitic oxide. J Am Chem Soc 80:1339

[33] Lee T, Yun T, Park B, Sharma B, Song HK, Kim BS (2012) Hybrid multilayer thin film supercapacitor of graphene nanosheets with polyaniline: importance of establishing intimate electronic contact through nanoscale blending. J Mater Chem 22:21092–21099

[34] Mondal K, Kumar R, Sharma A (2016) Metal-oxide decorated multilayered three-dimensional (3D) porous carbon thin films for supercapacitor electrodes. Ind Eng Chem Res 55:12569–12581

[35] Li Y, Wang H, Xie L, Liang Y, Hong G, Dai H (2011) MoS_2 nanoparticles grown on graphene: an advanced catalyst for the hydrogen evolution reaction. J Am Chem Soc 133:7296–7299

[36] Pastukhov AM, Skripchenko SY (2015) Process for recovering molybdenum and tungsten from MoS_3/WS_3 precipitates. Hydrometallurgy 157:78–81

[37] Klimova TE, Valencia D, Mendoza-Nieto JA, Hernández-Hipólito P (2013) Behavior of NiMo/SBA-15 catalysts prepared with citric acid in simultaneous hydrodesulfurization of dibenzothiophene and 4,6-dimethyldibenzothiophene. J Catal 304:29–46

[38] Bourne JR, Yu S (1994) Investigation of micromixing in stirred tank reactors using parallel reactions. Ind Eng Chem Res 33:41–55

[39] Pohorecki R, Bałdyga J (1988) The effects of micromixing and the manner of reactor feeding on precipitation in stirred tank reactors. Chem Eng Sci 43:1949–1954

[40] Chen JF, Zhou MY, Shao L, Wang YY, Yun J, Chew NYK, Chan HK (2004) Feasibility of preparing nanodrugs by high-gravity reactive precipitation. Int J Pharm 269:267–274

[41] Chen JF, Wang YH, Guo F, Wang XM, Zheng C (2000) Synthesis of nanoparticles with novel technology: high-gravity reactive precipitation. Ind Eng Chem Res 39:948–954

[42] Gigot A, Fontana M, Serrapede M, Castellino M, Bianco S, Armandi M, Bonelli B, Pirri CF, Tresso E, Rivolo P (2016) Mixed 1T-2H phase MoS_2/reduced graphene oxide as active electrode for enhanced supercapacitive performance. ACS Appl Mat Interfaces 8:32842–32852

[43] Chang K, Chen W (2011) In situ synthesis of MoS_2/-graphene nanosheet composites with extraordinarily high electrochemical performance for lithium ion batteries. Chem Commun (Cambridge) 47:4252–4254

[44] Chang K, Chen W, Ma L, Li H, Li H, Huang F, Xu Z, Zhang Q, Lee J-Y (2011) Graphene-like MoS_2/amorphous carbon composites with high capacity and excellent stability as anode materials for lithium ion batteries. J Mater Chem 21:6251–6257

[45] Yang X, Niu H, Jiang H, Wang Q, Qu F (2016) A high energy density all-solid-state asymmetric supercapacitor based on MoS_2/graphene nanosheets and MoS_2/graphene hybrid electrodes. J Mater Chem A 4:11264–11275

[46] Benavente E, Santa Ana M, Mendizábal F, González G (2002) Intercalation chemistry of molybdenum disulfide. Coord Chem Rev 224:87–109

[47] Wang C, Wan W, Huang Y, Chen J, Zhou HH, Zhang XX (2014) Hierarchical MoS_2 nanosheet/active carbon fiber cloth as a binder-free and free-standing anode for lithium-ion batteries. Nanoscale 6:5351–5358

[48] Chang K, Chen W (2011) Single-layer MoS_2/graphene dispersed in amorphous carbon: towards high electrochemical performances in rechargeable lithium ion batteries. J Mater Chem 21:17175–17184

[49] Liu D, Yu S, Shen Y, Chen H, Shen Z, Zhao S, Fu S, Yu Y, Bao B (2015) Polyaniline coated boron doped biomass derived porous carbon composites for supercapacitor electrode materials. Ind Eng Chem Res 54:12570–12579

[50] Li X, Li X, Cheng J, Yuan D, Ni W, Guan Q, Gao L, Wang B (2016) Fiber-shaped solid-state supercapacitors based on molybdenum disulfide nanosheets for a self-powered photodetecting system. Nano Energy 21:228–237

[51] Ma L, Ye J, Chen W, Chen D, Lee JY (2014) Gemini surfactant assisted hydrothermal synthesis of nanotile-like MoS_2/graphene hybrid with enhanced lithium storage performance. Nano Energy 10:144–152

[52] Cançado LG, Jorio A, Ferreira EM, Stavale F, Achete C, Capaz R, Moutinho M, Lombardo A, Kulmala T, Ferrari AC (2011) Quantifying defects in graphene via Raman spectroscopy at different excitation energies. Nano Lett 11:3190–3196

[53] Saraf M, Natarajan K, Mobin SM (2018) Emerging robust heterostructure of MoS_2–rGO for high-performance supercapacitors. ACS Appl Mater Interfaces 10:16588–16595

[54] Stoller M, Park S, Zhu Y, An J, Ruoff R (2008) Graphene-based ultracapacitors. Nano Lett 8:3498–3502

[55] Ke Q, Wang J (2016) Graphene-based materials for supercapacitor electrode—a review. J Materiomics 2:37–54

[56] Jose SP, Tiwary CS, Kosolwattana S, Raghavan P, Machado LD, Gautam C, Prasankumar T, Joyner J, Ozden S, Galvao DS, Ajayan PM (2016) Enhanced supercapacitor performance of a 3D architecture tailored using atomically thin rGO–MoS_2 2D sheets. RSC Adv 6:93384–93393

[57] Chang BY, Park SM (2006) Integrated description of electrode/electrolyte interfaces based on equivalent circuits and its verification using impedance measurements. Anal Chem 78:1052–1060

[58] Stoller MD, Ruoff RS (2010) Best practice methods for determining an electrode material's performance for ultracapacitors. Energy Environ Sci 3:1294–1301

[59] Hulicova-Jurcakova D, Puziy AM, Poddubnaya OI, Suárez-García F, Tascón JM, Lu GQ (2009) Highly stable performance of supercapacitors from phosphorus-enriched carbons. J Am Chem Soc 131:5026–5027